RSC Advances

PAPER

Cite this: *RSC Adv.*, 2019, **9**, 21911

Porous 3D flower-like CoAl-LDH nanocomposite with excellent performance for NO_2 detection at room temperature†

Zhi Liu,[a] Lei Teng,[a] Laifeng Ma,[a] Yang Liu,[a] Xueying Zhang,[a] Jialing Xue,[a] Muhammad Ikram,[a] Mohib Ullah,[a] Li Li*[ab] and Keying Shi *[a]

Received 13th April 2019
Accepted 9th July 2019

DOI: 10.1039/c9ra02799h

rsc.li/rsc-advances

The 3D flower-like CoAl-layered double hydroxide (CoAl-LDH) was successfully prepared using the functional template agent of fluoride ions *via* a facile one-step hydrothermal route. Various techniques proved that all the samples presented 3D flower-like microstructural morphology. Representatively, the CA-2 sample, which was synthesized with the molar ratio of Co : Al of 3.65 : 1, had considerably abundant pores in its thin nanosheets. The average pore size was 2–4 nm, the specific surface area was equal to 49.45 $m^2\ g^{-1}$, and the thickness of nanosheets was approximately 3.068 nm. The CA-2 sample showed an excellent response to 0.01–100 ppm NO_2 with ultrafast response/recovery time at room temperature (RT). The detection limit of the sensor even reached 10 ppb. The superior gas sensing performance could be attributed to the synergistic effects of the functional template agent of fluoride ions and specific porous 3D flower-like nanostructure. The current study showed that the 3D flower-like CoAl-LDHs might a promising material in practical detection of NO_2 at RT.

Introduction

As a notorious gas, nitrogen dioxide (NO_2) plays a central role in the formation of photochemical smog, acid rain and PM2.5 as well as ozone formation in the atmosphere.[1–3] According to the National Institute for Occupational Safety and Health, NO_2 may cause harm to life at concentrations higher than 20 ppm.[4] Faced with this, the sensitive monitoring of NO_2 is extremely important to public health and the environment. Many NO_2 sensing materials such as SnO_2,[5,6] TiO_2,[7,8] WO_3,[9,10] and ZnO[11] have been investigated as solid-state gas sensor materials. Khuspe *et al.*[6] prepared nanostructured SnO_2 to detect NO_2 gas at 200 °C. 3D hierarchical flower-like WO_3 was applied by Wang *et al.*[9] to detect NO_2 at 100 °C. Using ZnO nanorods/TiO_2 materials, Zou *et al.*[11] studied their detection of NO_2 gas at 180 °C. Many efforts have been made to improve NO_2 gas detecting sensors,[12–14] but there are still some problems such as low sensitive response and high energy consumption.

Recently, two dimensional (2D) layered materials have become attractive in gas sensing because of being tunable and functionable.[15,16] As typical 2D materials, LDHs have been exploited for abundant applications ranging from catalysis[17,18] to electrochemistry[19] and gas sensing.[20,21] In LDHs, A^{n-} anions are located in the interlayer gallery to balance positively charged brucite-like host layers of edge-sharing MO_6 octahedra;[22–27] notably, hydrogen bonds inside the interlayer space can provide an interacting site for external molecules,[28] therefore, LDHs lately has been used as gas sensing materials.[29] Table 1 showed a comparison of the gas sensing characteristic of LDHs reported in the literature and in present work. From this table, it was observed that Morandi *et al.*[20] reported Pt/Zn/Al-LDH as CH_4 gas sensor material operating at 450 °C, not only consumed too much energy, but also increased cost by using precious metal. $(ZnAl\text{-}LDH/PAN)_n$ as NH_3 sensor at RT was investigated by Xu *et al.*,[30] which faced a number of difficulties including complex preparation process and long response/recovery time. Our previous reported work,[21] reported an MgAl-LDH based gas sensor for NO_x gas detection at RT, but there were still some shortcomings such as lower sensitivity and detection limit only at ppm level.

In this work, to further improve gas sensitivity, a 3D flower-like CoAl-LDHs nanocomposite with ultra-thin nanosheets (NSs) was synthesized *via* a simple hydrothermal method. Fluoride ion was utilized as a functional template agent under mild conditions. The functionalized composite was systematically characterized. One of sample showed excellent performance of high sensitivity, and ultra-fast response/recovery. Its detection limit was able to reach ppb level. Synthetic approach and related properties of newly-synthesized were discussed in detail.

[a]*Key Laboratory of Functional Inorganic Material Chemistry, Ministry of Education, School of Chemistry and Material Science, Heilongjiang University, Harbin, 150080, P. R. China. E-mail: shikeying2008@163.com*

[b]*Key Laboratory of Chemical Engineering Process & Technology for High-efficiency Conversion, Heilongjiang University, Harbin, 150080, P. R. China*

† Electronic supplementary information (ESI) available. See DOI: 10.1039/c9ra02799h

Table 1 Comparison of the gas sensing characteristics of LDHs reported in literature and in present work

Sensor material	Operating temperature	Gas	Gas concentration	Response	Response time	Recovery time	Ref.
Pt/ZnAl-LDH	450 °C	CH_4	500 ppm	5	—	—	20
ZnAl–calcein-LDH	80 °C	Ethanol	100 ppm	5	—	—	30
Ag/MgAl-LDH	RT	Ethanol	200 ppm	7.8	10 s	50 s	31
ZnAl-LDH/PANI	RT	NH_3	1000 ppm	16	150 s	240 s	32
NiAl-LDH	RT	O_3	700 ppb	1.84	8 s	74 s	33
HPTS/NiFe-LDH	RT	CO_2	—				34
MgAl-LDH	RT	NO_x	100 ppm	76%	1.3 s	—	21
CoAl-LDH	RT	NO_2	100 ppm	26.61	1.3 s	14.6 s	This work

Experimental

Materials and chemicals

All of the chemical reagents used in the experiment were analytical grade as purchased and be used directly without any further purification. $Co(NO_3)_2 \cdot 6H_2O$, $Al(NO_3)_3 \cdot 9H_2O$ and urea were purchased from Xilong Chemical Co., Ltd., NH_4F was purchased from Beijing Yili Fine Chemical Co., Ltd.

Synthesis of functionalized CoAl-LDHs

Functionalized CoAl-LDHs were synthesized through a urea hydrolysis reaction without any surfactant. 0.8 mmol $Co(NO_3)_2 \cdot 6H_2O$ (0.233 g), 0.4 mmol $Al(NO_3)_3 \cdot 9H_2O$ (0.15 g), 4 mmol NH_4F (0.15 g) and 28 mmol urea (1.7 g) were mixed in 40 mL deionized water and the mixed solution was continuously stirred for 0.5 h. The solution was then moved into a 50 mL Teflon-lined stainless steel autoclave. It was subsequently sealed, put into the electric blower drying box and heated at 90 °C for 6 h. Until being cooled naturally to room temperature, the obtained pink CoAl-LDHs was thoroughly washed with deionized water and ethanol. It was dried at 60 °C in air for 12 h and named as CA-2 (the molar ratio of Co : Al = 3.65 : 1). In addition, changed amount of $Co(NO_3)_2 \cdot 6H_2O$ (0.4 mmol, 0.117 g) and (1.2 mmol, 0.349 g), and resulting samples were labelled as CA-1 (the molar ratio of Co : Al = 3.40 : 1), CA-3 (the molar ratio of Co : Al = 3.80 : 1). It should be noted that the synthetic condition was the same as CA-2. CAW was a sample without adding NH_4F. By varying hydrothermal time *i.e.* from 1 to 5 hours, five different samples were obtained (see Fig. S2a†). The specific synthetic condition was listed in Table S1.†

Materials characterizations

Crystalline structure and chemical composition of the samples were characterized through X-ray powder diffraction (XRD, Rigaku TTRIII X-ray diffractometer, $\lambda = 1.5406$ Å) and Fourier transform infrared spectroscopy (FT-IR, Varian FTIR spectrophotometer), respectively. The morphology and size of the products were studied by scanning electron microscopy (SEM, HITACHI S-4800) and transmission electron microscopy (TEM, JEOL JEM-2100) at an accelerating voltage of 200 kV. Specific surface areas and pore size distribution of the samples were performed by using the Brunauer–Emmett–Teller (BET). Chemical state of elements in composite were studied by using X-ray photoelectron spectroscopy (XPS). The charge transfer and carrier concentration were evaluated by electrochemical impedance spectroscopy (EIS) and Mott–Schottky (MS) plot using electrochemical working station (CHI660C, Shanghai, China) at room temperature. Temperature program desorption (TPD) studies was performed by AutoChem TP5080 chemisorption analyzer with a temperature ramp of 10 °C min^{-1}, and using mass spectra (QIC-20, Hidden) to record TPD signals.

Fabrication and testing of gas sensor

Manufacture method of CoAl-LDHs composites sensor film and test measurement were similar to our reported previously.[21] Sensor resistance test was performed at room temperature (RT = 25 °C) and a relative humidity (RH = 26%). After NO_2 reacted with the sensor to get a response, fresh air was injected and started to recover. The response was calculated as follows:

$$R = R_a/R_g$$

where R_a and R_g represent resistance in air and target gas respectively. The response and recovery time are defined as time taken to reach 90% of resistance change value. Repeatability was studied by using four sensors under each sensor detection.

Results and discussions

As demonstrated in Scheme 1a, urea, a common ammonia-releasing agent, was utilized as pH buffer to release OH^- slowly and constantly, and provided carbonate ions simultaneously during the hydrolysis.[35] This offers the basic environment to precipitate Co^{2+}, yet it might prevent oxidation of Co^{2+} because of its reducibility. Moreover, F^- played the role of functional template agent in formation of LDHs.[36–38] During the hydrothermal reaction, a large number of particles came into being and formed microspheres over time, which taken the juts on the surface of microspheres as crystal nucleus and further grew into nanofibers with F^- as structure-orientation agent under the unreacted urea solution. The steric hindrance and magnetic interaction forced nanofibers to orient radially,[39] and the urchin-like grew up slowly (Scheme 1b), eventually formed in 3D flower-like structure (Scheme 1c). The main reactions in the precursor solution were described as follows:[40,41]

$$NH_2CONH_2 \rightarrow NH_4^+ + CNO^- \quad (1)$$

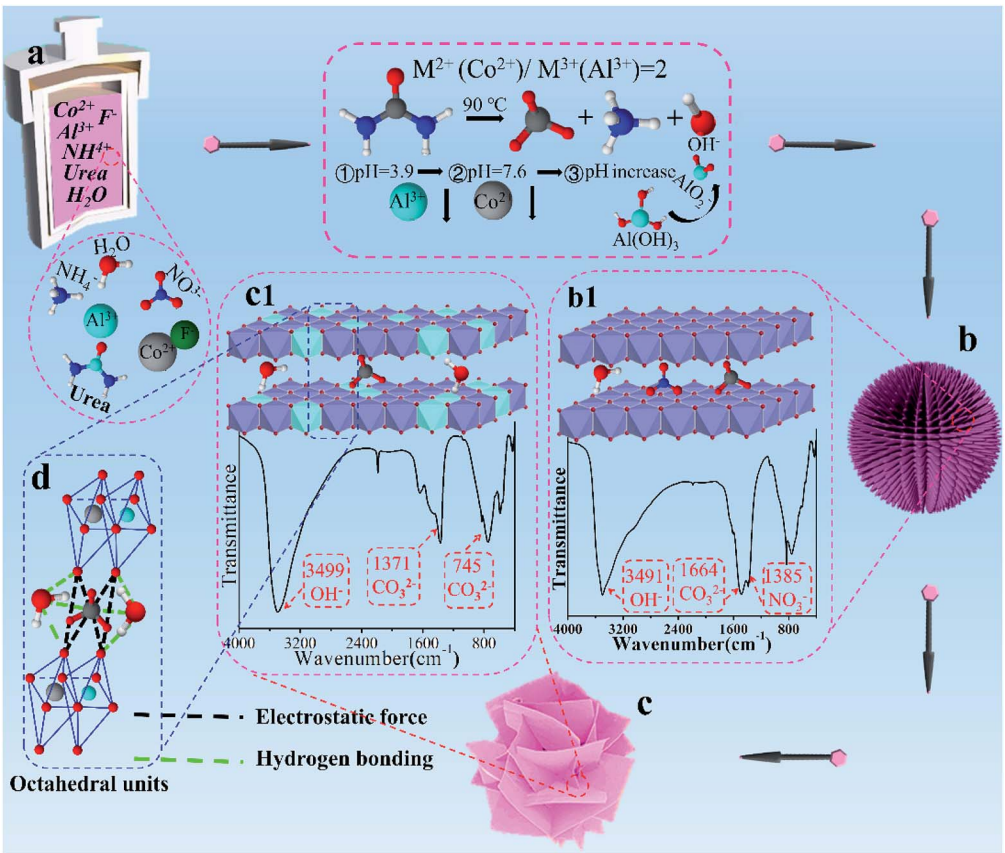

Scheme 1 The formation mechanism of functionalized 3D flower-like CoAl-LDH (a) precursor solution containing Co^{2+}, Al^{3+}, F^{-}, NH^{4+} and urea; (b and b1) C-2; (c and c1) CA-2; and (d) octahedral units of CA-2.

$$CNO^{-} + 3H_2O \rightarrow HCO_3^{-} + NH_4^{+} + OH^{-} \quad (2)$$

$$NH_2CONH_2 + H_2O \rightarrow 2NH_3 + CO_2 \quad (3)$$

$$NH_3 + H_2O \rightarrow NH_4^{+} + 2OH^{-} \quad (4)$$

In the reaction process, pH gradually increased with slow hydrolysis of urea. At the beginning of crystallization, continuous hydrolysis was in favor of precipitation of $Al(OH)_3$ due to the pH value of Al^{3+} (pH = 3.9) was lower than that of Co^{2+} (pH = 7.6).[42] However, there were no diffraction peaks of aluminum hydroxide or hydrous oxide appearance (Fig. S2a†), that is, Al^{3+} first formed AlO_2^{-} in alkali aqueous. Then the complexation between AlO_2^{-} and OH^{-} occurred to produce $[Al_{13}(OH)_{32}(H_2O)]^{7+}$.[43] During this process, α-$Co(OH)_2$ was formed in approximately 1 h (Fig. S2a†), which contained carbonate ions and nitrate ions in the interlayer gallery (Scheme 1b1). With reaction time increasing, Al^{3+} complex in $[Al_{13}(OH)_{32}(H_2O)]^{7+}$ would promptly transport into the lattice of α-$Co(OH)_2$ and substitute Co^{2+} to form CoAl-LDH nanosheet (Fig. S2c†).[43,44] This attributed to the ionic radius of Al^{3+} (0.053 nm) was lower than that of Co^{2+} (0.070 nm), eventually formed ultrathin nanosheets (Scheme 1c) with carbonate ions intercalated into 3D flower-like CoAl-LDH.

To investigate the crystal structure and purity of samples, XRD of CoAl-LDHs after hydrothermal reaction was depicted in Fig. 1a. The study showed that all XRD peaks for CoAl-LDHs could be indexed in a hexagonal cell (a = 0.308 nm, c = 2.301 nm) with the rhombohedral symmetry $R3m$. Interlayer spacing (d_{003} = 0.767 nm) proved that carbonate anion intercalated in LDHs. The existence of carbonate anions was likely produced from urea hydrolysis in the hydrothermal process. There were four characteristic diffraction peaks with equal spacing at 11.6°, 23.32°, 34.25° and 46.27°, corresponding to (003), (006), (012) and (018) crystal planes (CoAl-LDHs JCPDS: 51-0045), respectively. The typical doublet (110) and (113) crystal planes of CoAl-LDHs could be clearly observed within the scope of 2θ = 60–62°. The diffraction peaks of (003), (006) crystal planes were stronger compared with the other peaks indicating that CoAl-LDHs grew along an axial direction during the formation. Furthermore,

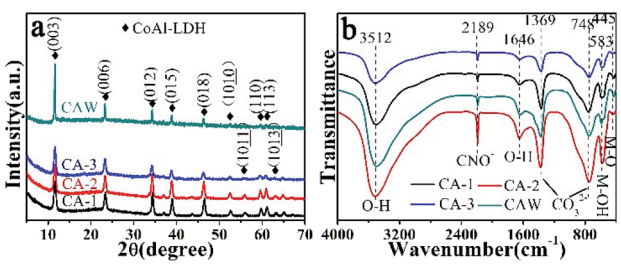

Fig. 1 XRD diffraction pattern (a) and FT-IR spectra (b) of CA-1, CA-2, CA-3 and CAW.

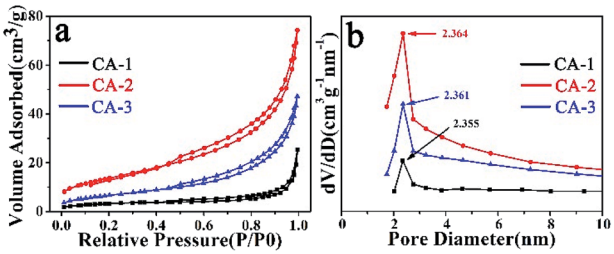

Fig. 2 BET (a) and BJH (b) curves of CA-1, CA-2 and CA-3.

there were two diffraction peaks (10$\underline{11}$) and (10$\underline{13}$) appeared after using F^- as functional template agent. This may be due to the effect of functional F^- controlling the crystal structure. On the other hand, no other peaks appeared, which clearly indicated that high purity of CoAl-LDHs were formed during preparation process.

FT-IR spectrum was carried out to investigate the chemical composition of CoAl-LDHs (Fig. 1b). There were four characteristic peaks associated with CoAl-LDH. The broad band at 3512 cm^{-1} belonged to O–H stretching vibration from H-bonded OH group and water molecules in the interlayer.[45] The peak at 1646 cm^{-1} could be assigned to the bending mode of interlayer water molecule. The peaks at 1369 and 748 cm^{-1} corresponded to ν_3 bending vibration of CO_3^{2-} indicating that carbonate ions had been intercalated into LDHs. The low frequency peak at 583 cm^{-1} was attributed to the M–OH bending mode of Co and Al, and 445 cm^{-1} could be assigned to M–O stretching vibration.[46] Furthermore, the narrow peak appeared at 2189 cm^{-1} was the typical stretching vibration of C≡N bonds in CNO anions indicating the incomplete decomposition of urea.[47]

The specific surface area and pore size distributions of the as-synthesized composites CA-1, CA-2 and CA-3 were investigated by using BET technique. The detailed information was presented in Fig. 2 and Table S2.† All the three samples represented typical IV isotherms with H3 type hysteresis loop, which made clearly the presence of mesoporous structure. According to the pore size distribution curve, there was very slight change in the distribution centers. The pore size distribution was about 2–4 nm. Relative to other two samples, the CA-2 possessed the largest surface area (49.45 $m^2 g^{-1}$) and its total pore volume was 0.10 $cm^3 g^{-1}$. High pore volume could provide a delivery channel for electron easily transmitted to internal space, which was beneficial for NO_2 gas sensing. This meant CA-2 would process higher NO_2 sensitivities.

Morphology of the samples was examined by SEM and TEM. SEM images of the as-prepared CA-1, CA-2 and CA-2 samples were shown in Fig. 3. Fig. 3a–f distinctly revealed that the morphologies of CA-1, CA-2, and CA-3 not similar to each other. When the molar ratio of Co : Al was much lower, the morphology of CA-1 was insufficient to support formation of flawless nanosheets (Fig. 3b). When the molar ratio of Co : Al was much higher, excess primitives of CA-3 were attached to spaces between the neighboring nanosheets to form microscopic nanostructures (Fig. 3f). The CA-2 sample with the optimal ratio of Co : Al displayed a 3D flower-like structure (Fig. 3d), which was composed of a large number of well-dispersed ultrathin nanosheets, and there was a lot of interspaces between the layered nanopetals and thin nanosheets. The as-prepared CAW sample presented well-defined nanosheet structure was shown in Fig. S4.†

As shown in Fig. 4, low magnification TEM images of CA-2 demonstrated that 3D flower-like nanostructure was formed and the sample consisted of many ultrathin nanosheets with mesoporous size about 2–4 nm. The formation of mesoporous attributed to the release of CO_2 during the urea hydrolysis process, and it was beneficial to improve the gas sensing properties.

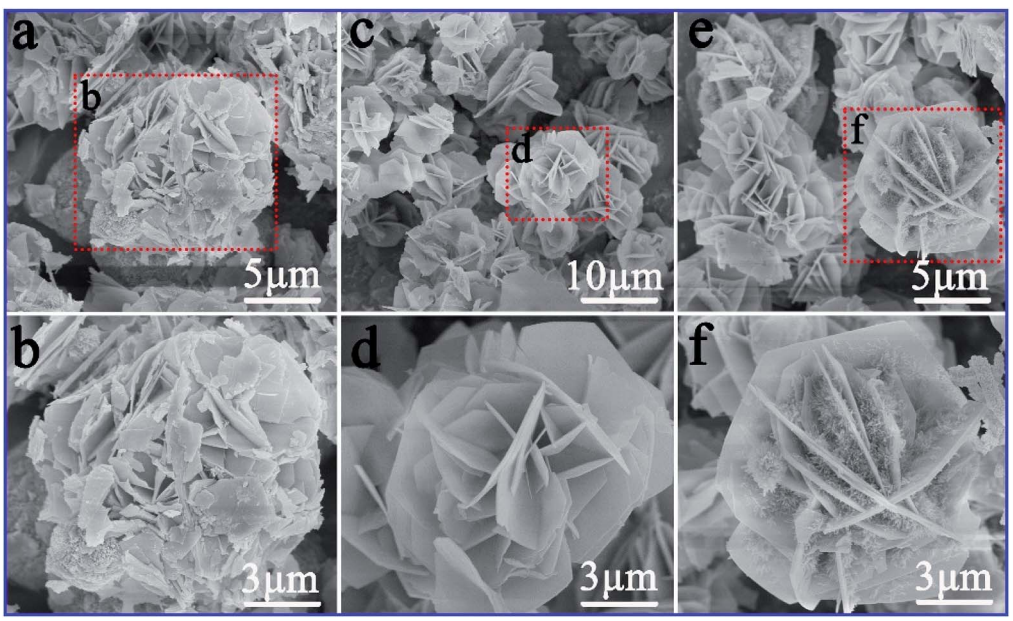

Fig. 3 SEM images of CA-1, CA-2 and CA-3.

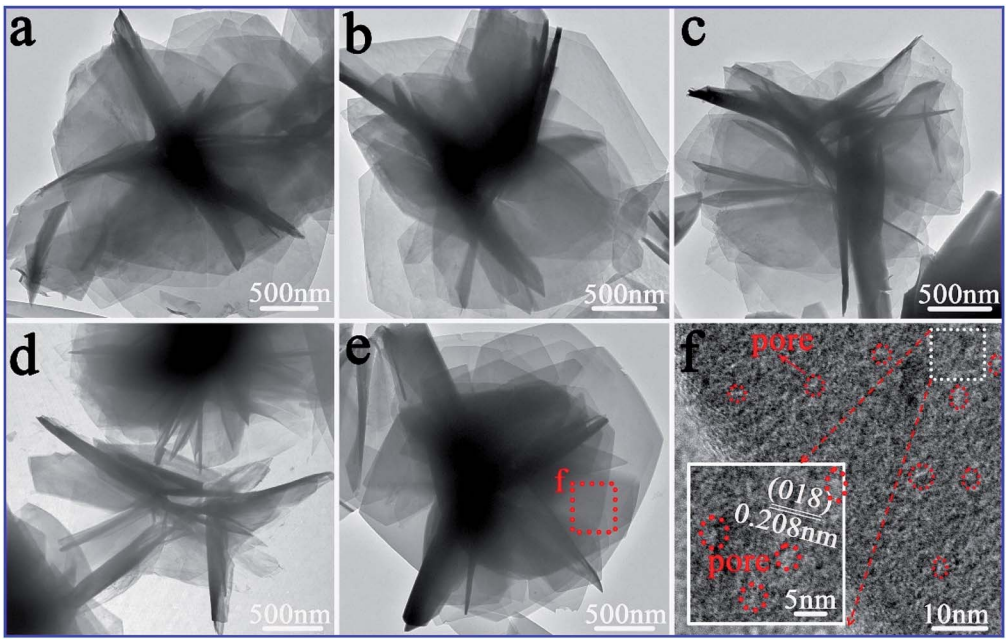

Fig. 4 TEM images of the CA-2 sample (a–e), together with a HRTEM image (f) from the (e) picture.

As illustrated in Fig. 5a, CA-2 sample was composed of many 3D flowers with the size of 2.4–3.4 μm. The well-defined flower clearly illustrated that abundant nanosheets (Fig. 5b) were assembled to form a 3D flower-like architectures. Petals in Fig. 5c further confirmed the flowers consisted of uniform and ultrathin nanosheets with 4.0 layers and thickness of 3.068 nm. Moreover, as shown in HRTEM of Fig. 5d and e, the value of the interplanar spacing between the adjacent lattice fringes were 0.235 and 0.391 nm, which were consistent with (015) and (006) planes of CoAl-LDHs, respectively. The polycrystalline diffraction rings (Fig. 5f) from inside to outside were (015), (018) and (113) planes, respectively, which in accordance with the results of XRD (Fig. 1a). TEM and HRTEM images of CAW sample shown in Fig. S5† confirmed that the as-preparation sample with nanosheet structure has low crystallinity.

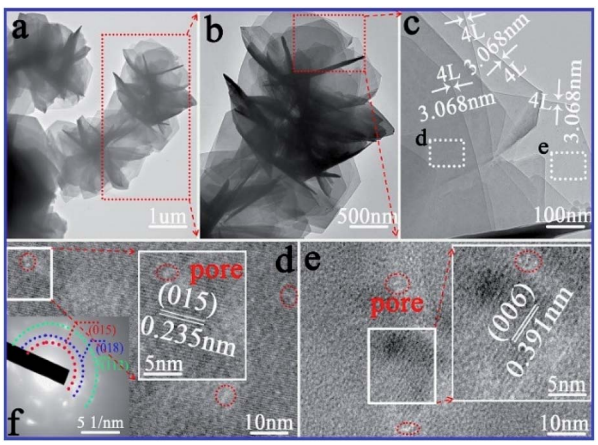

Fig. 5 Microstructure of CA-2: (a–c) gradually enlarged TEM images, (d and e) HRTEM images of different compositions, and (f) SAED pattern.

The element mapping and EDS spectra of CA-2 were used to verify the element distribution (Fig. 6). The bright image in Fig. 6b–e indicated that Co, Al, O and F elements were distributed uniformly. As Fig. 6f showed that Co atomic element contents was 26.49%, Al 7.24%, O 57.73%, and F 8.54%. The atomic ratio of Co/Al in CA-2 was calculated to be 3.65 : 1.

To reveal the surface chemical composition and the element electronic states of the flower-like CoAl-LDHs, the corresponding XPS results were presented in Fig. 7. Fig. 7a–c depicted the high-resolution Co 2p spectrum in CoAl-LDHs. For comparison, distributions of Co 2p XPS peaks were similar in three samples. The peaks of Co $2p_{3/2}$ was at 781.9, 781.7 and 781.8 eV, and Co $2p_{1/2}$ at 797.3, 797.2 and 797.2 eV, with the spin–orbit splitting value of 15.4, 15.5 and 15.4 eV, respectively. These all proved that Co ion existed in the form of $Co(OH)_2$. The other three satellite bands demonstrated that Co ion existed in the form of divalent Co^{2+} state.[48,49]

In the O 1s spectra (Fig. 7d–f), the spectra could divide into two peaks by using Gaussian fitting. Binding energy at 530.9 eV (peak 1) could be attributed to Co–OH and/or Al–OH groups,[50] indicating there was a large amount of OH groups inside the interlayer which could provide an interaction site for external molecules. The peak 2 (532.2–532.6 eV) could be attributed to chemisorbed oxygen.[51] The calculated chemisorbed oxygen of CA-1, CA-2 and CA-3 was about 18.64%, 24.91% and 20.19% (Table S3†), respectively, and CA-2 sample had the largest calculated chemisorbed oxygen. More chemisorbed oxygen participated in surface reactions, the higher response sensitivity might be produced.

Al 2p spectrum was presented in Fig. 7g–i. It could be concluded that there was only Al^{3+} species peaks existed in CoAl-LDHs (BE = 72.9–73.0 eV).[52]

XPS spectrum of F^- in 682–692 eV (Fig. 7j–l) clearly indicated that the substitution of OH^- by F^- did not cause a large lattice

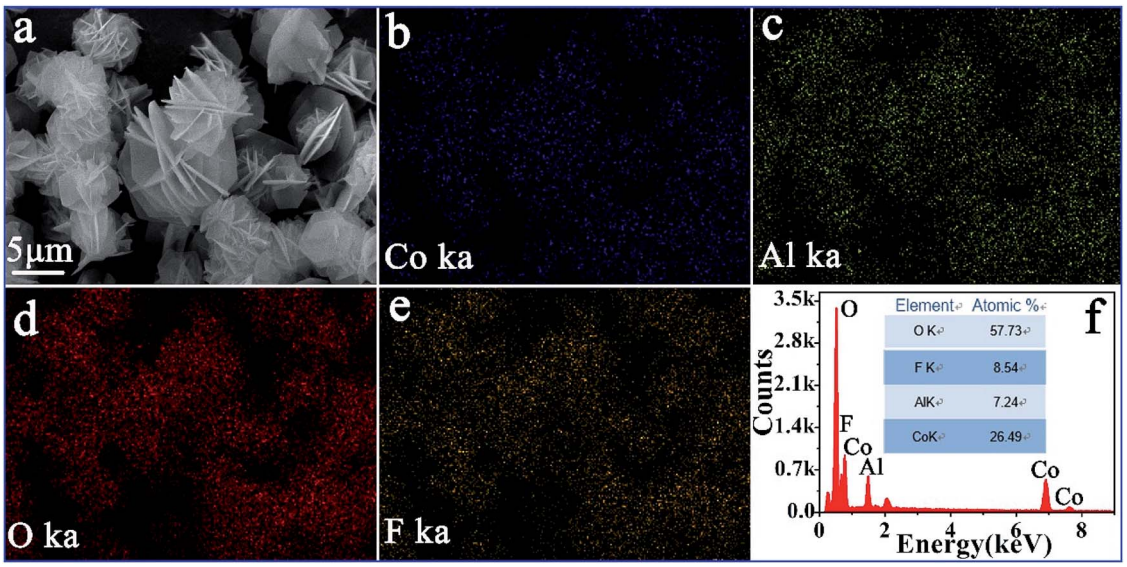

Fig. 6 SEM image/EDS mapping of CA-2: (a) bright field image, (b–e) Co, Al, O and F element mapping, and (f) EDS spectra.

distortion because ionic radius of F^- (0.117 nm) was similar to that of OH^-.[53] The existence of fluoride ions (F^-) enhanced carrier concentration and decreased charge transfer resistance.[54,55] This result was consistent with those of MS (Fig. 9e) and EIS (Fig. 9f).

Enhanced NO_2 gas sensing properties

For comparison, gas sensing properties to NO_2 were investigated for CA-1, CA-2 and CA-3 based sensors at RT, as shown in Fig. 8.

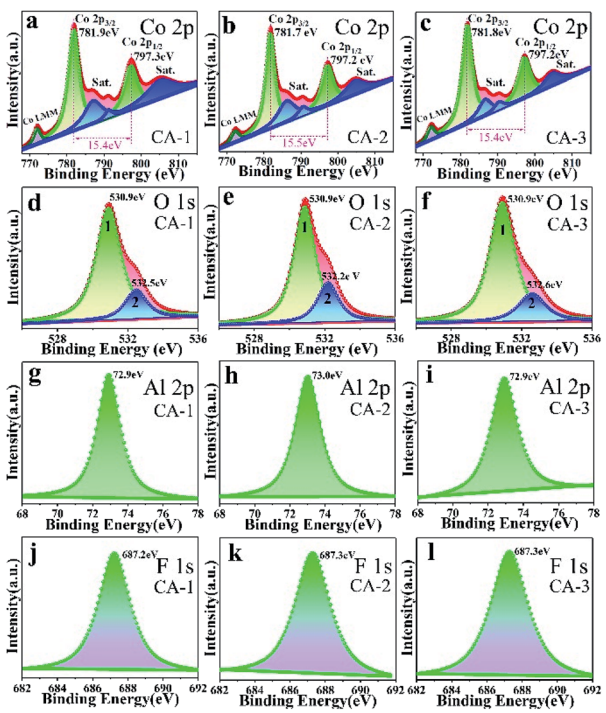

Fig. 7 XPS spectra of CA-1, CA-2 and CA-3 samples: (a–c) Co 2p, (d–f) O 1s, (g–i) Al 2p, and (j–l) F 1s.

As shown Fig. 8a, the CA-2 sensor shown the maximum response towards 100 ppm NO_2 was 26.61, which was 5.03 and 1.3 times higher than that of CA-1 and CA-3 sensor, respectively. Their detection limit towards NO_2 all could reach to 0.01 ppm, and the response of CA-2 was significantly higher than that of other two sensors, as Table S4† summarized. Fig. S6† presented that slope of the response curve was higher for low concentration than high concentration of NO_2. This further illustrated that CoAl-LDHs based sensor possessed a great ability to detect low concentration NO_2.

Fig. 8b and c showed response/recovery time of CA-1, CA-2 and CA-3 based sensors at RT under different NO_2 concentration. The response time tended to increase while the recovery time was the opposite. It was worth noting that the response time of the CA-2 sensor was only 1.3 s (Table S4†) at 100 ppm, faster than that of the other two sensors. Even at the lowest detection limit (10 ppb), the response time of CA-2 sensor was still the shortest (4.6 s). Moreover, it could be clearly observed that the recovery time of CA-2 sensor was faster than that of other two sensors at every NO_2 concentration (Table S4†). This was further verified by NO_2-TPD (Fig. 8d and S7†). Compared with the other two samples, the physical desorption peak of CA-2 sample shifted towards lower temperature with a larger area. This indicated that CA-2 possessed a high adsorption capacity for NO_2 at RT (25 °C), which was conductive to the desorption process at lower temperature.[56,57]

To further investigated the gas sensing properties of CA-2 sensor, selectivity, repeatability, stability, MS and EIS tests were carried out at RT as presented in Fig. 9.

Fig. 9a depicted the dynamic response–recovery curve of CA-2 sensor at RT under different concentration of NO_2. When NO_2 was injected and reacted with CA-2 sensor, its resistance dropped rapidly to a minimum value in a short time, and recovered back to its initial value after purging the gas with fresh air. The response gradually reduced with the injected concentration of NO_2 decreasing and ultimately reached to a lower limit detection of 0.01 ppm.

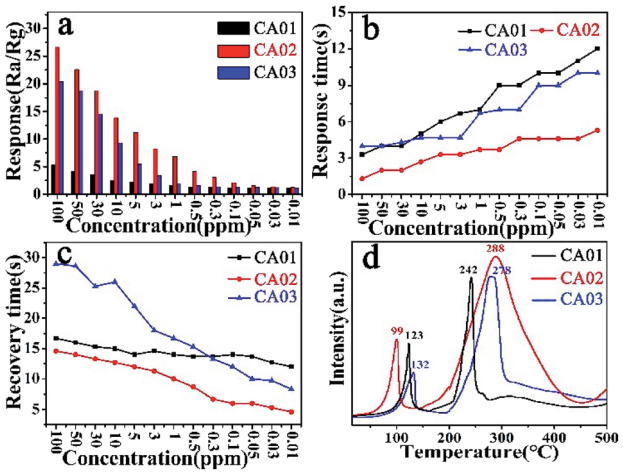

Fig. 8 (a) Response; (b) response time; (c) recovery time and (d) NO_2-TPD of the CA-1, CA-2 and CA-3 sensor.

Fig. 9b showed that CA-2 sensor almost had no response to five detection gases (*e.g.* NH_3, CO, CH_4, H_2 and H_2S) at RT, but significantly higher response to NO_2, demonstrating that it had an excellent selectivity toward NO_2.

It was well-known that repeatability and long-term stability were vitally important parameters for sensor devices. As illustrated in Fig. 9c, response–recovery curves of CA-2 resistance to 10 ppm of NO_2 at RT maintained the initial resistance upon 30 cycles without a clear attenuation, this revealed the sensor's stable and repeatable character. In addition, the measurement of the response values of CA-2 sensor to 10 ppm NO_2 at RT and its initial resistance in air atmosphere (R_a) for 54 days further verified its excellent long-term stability in Fig. 9d.

Generally, low resistance and superior electron transportation are critical to sensitive materials.[58] MS plot measurements were performed to investigate electric characteristics of CoAl-LDHs. As Fig. 9e showed, slope of CoAl-LDHs's plot was negative, indicating CoAl-LDHs exhibited a p-type behavior. Based on the calculation,[59] carrier concentration of CA-1, CA-2, CA-3 and CAW were 2.31×10^{15}, 9.80×10^{15}, 5.82×10^{15} and 3.08×10^{15} (Table S7†), respectively, and CA-2 had the largest carrier concentration of 9.80×10^{15}.

EIS measurements were carried out to study charge-transfer of the samples. As shown in Fig. 9f, CA-2 sample had the smallest semicircle radii. The relevant equivalent circuit model and the impedance parameters' results were given in Fig. S9 and Table S7.† It was well known that radius of high-frequency region was thought to be associated with charge transfer, and the smaller radius means lower resistance. Consequently, EIS results indicated that CA-2 had a superior charge transport property, which could provide an ideal electron transmission.

Gas sensing mechanism

LDHs commonly had a large surface/volume ratio and their structures proved to be able to absorb detection gases because of its interlayer spacing could use as a gallery pathway. What's more, the hydrogen bond between surface hydroxyl group and interlayer water molecules was equivalent to bridge connecting the adjacent the positively charge layers. This bridging effect could provide natural channels for the effective and fast transportation of carriers.

It was known that gas sensing mechanism of solid-state sensors could be attributed to modulation of electrical conductivity on the surface in the presence and absence of the target gas.[60,61] The mechanism of NO_2 sensing for CoAl-LDHs was proposed in Scheme 2 which predominantly showed the involvement of three steps: adsorption, charge transfer and desorption process.

In air (Scheme 2a), surface electrons of the samples were captured by O_2 from accepter level of the sensor, leading to the formation of ionized O_2^-. As a result, decreased the conductivity and enhanced the resistance of the sensing material (eqn (5) and (6)):[62]

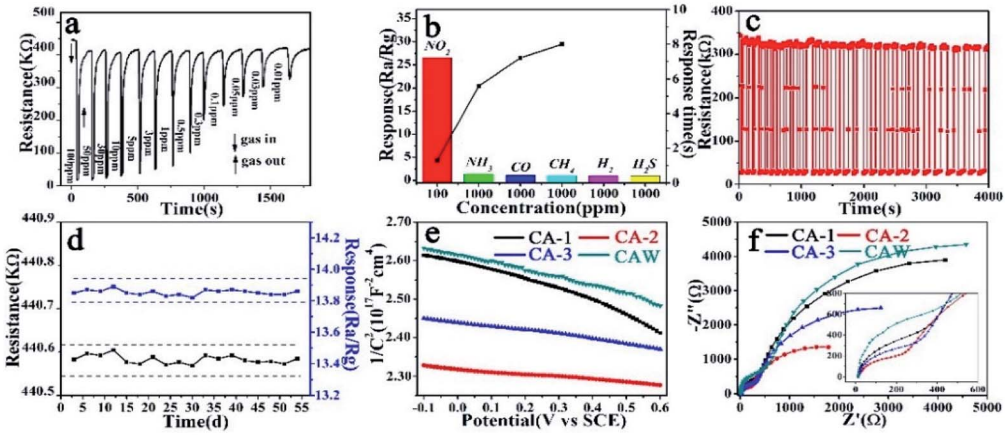

Fig. 9 Sensing properties (a) dynamic response–recovery curve of the CA-2 sensor for 100–0.01 ppm at RT; (b) response of CA-2 sensor for different gas; (c) thirty cycles of dynamic response curves of CA-2 sensor to 10 ppm NO_2; (d) stability of CA-2 sensor to 10 ppm NO_2 for 54 days at RT; (e) Mott–Schottky plots of CA-1, CA-2, CA-3 and CAW modified electrodes in 1 M KOH electrolyte measured at a frequency of 1 kHz; (f) EIS of CA-1, CA-2, CA-3 and CAW.

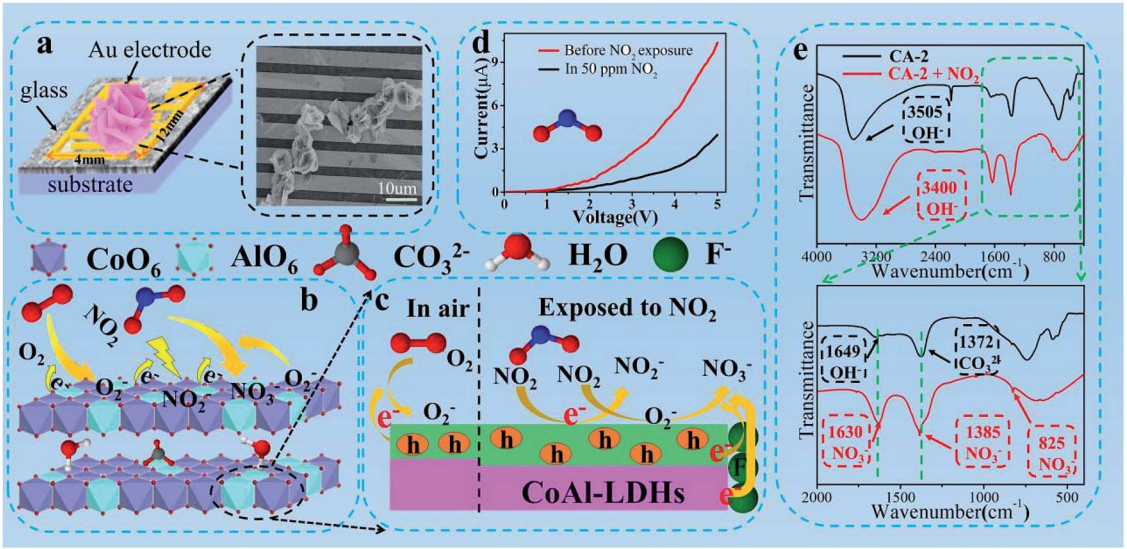

Scheme 2 Schematic for the mechanism of NO_2 sensing for CoAl-LDHs. (a) SEM image of 3D flower-like CA-2 on Au electrode; (b and c) the model with response procedure of gas sensing; (d) *I*–*V* curve measured for CA-2 sensor in air and 50 ppm NO_2 exposure at RT; (e) IR spectra of CA-2 before and after NO_2 gas detection (CA-2 test NO_2 gas sensing for 2 h).

$$O_{2(gas)} \leftrightarrow O_{2(ads)} \quad (5)$$

$$O_{2(ads)} + e^- \rightarrow O_{2(ads)}^- \quad (6)$$

where "ads" means the "adsorbed".

As shown in Scheme 2b and c, when the samples were exposed to NO_2, the gas molecules not only captured free electrons from the accepter electron level of CoAl-LDHs to produce NO_2^-, but also reacted with O_2^- forming NO_3^-, which led to an increase in the hole density and ultimately a rapid decrease in the resistance (eqn (7) and (8)).

$$NO_{2(gas)} + e^- \rightarrow NO_{2(ads)}^- \quad (7)$$

$$NO_{2(gas)} + O_{2(ads)}^- + 2e^- \rightarrow NO_{3(ads)}^- + 2O_{(ads)}^- \quad (8)$$

Scheme 2d showed the *I*–*V* plots for CA-2 sensor exposure to 50 ppm NO_2 gas. It was worth noting that the current was decreased when CA-2 sensor exposure to NO_2 gas. Because of the oxidation of NO_2, it was easily adsorbed on the surface of CA-2 and withdrew electrons from CA-2. This led to the electron carrier concentration decreasing and significantly changed the resistance.

Therefore, 3D flower-like CA-2 sensor presented an outstanding NO_2 gas sensing performance at RT, especially high response, short response/recovery time. This could be ascribed to the following factors: first, the morphology of 3D flower-like CA-2 consisted of ultrathin nanosheets in its framework. Its thickness was 3.068 nm, which was in favored of the electrons transfer speed from internal to surface; second, there were a large number of mesoporous existed on the surface of ultrathin nanosheets which facilitated the gas diffusion/adsorption alleyway. NO_2 gas could be easily adsorbed at the outer/inner surfaces as well as the entire mesoporous wall. In addition, the largest specific surface area of CA-2 provided a number of active sites, which provided more oxidative NO_2 molecules absorbed sites and finally led to the high response. In particularly, as functional template agent, the roles of fluoride ions (F^-) (i) decreased the charge transfer resistance (Fig. 9f and Table S7†), *i.e.* the electron would transfer faster in adsorption and desorption process; (ii) enhanced the carrier concentration (Fig. 9e and Table S7†), which meant there were more electrons would react with oxygen to produce more O_2^-. These were all beneficial for the high response of CA-2.

Conclusions

In summary, a facile one-step hydrothermal method was developed to synthesize a 3D flower-like CoAl-LDHs architecture by using fluoride ion as a functional template agent. Specifically, the morphology of the functionalized 3D flower-like CA-2 sample consisted of ultrathin nanosheets with 3.068 nm thick in its framework, and a large number of mesoporous existed on the surface of ultrathin nanosheet. A systematic and comparative analysis indicated that the CA-2 based sensor showed a notable NO_2 gas sensing performance at RT, *i.e.*, high sensitivity, fast response/recovery time, and detection limit of ppb level. The superior performance was attributed to the 3D flower-like morphological and mesoporous structure of CoAl-LDHs as well as the fluoride ion as functional template agent. The existence of fluoride ion decreased the charge transfer resistance and enhanced the carrier concentration which led to much higher sensing response. Therefore, the functionalized CA-2 sample, displayed an outstanding sensing activity to super low-concentration NO_2 gas at RT, it would be a potential candidate to fabricate relevant sensor. And our facile synthetic method could be a promising method to prepare the basic gas sensor materials.

Conflicts of interest

There are no conflicts to declare.

Acknowledgements

This work was supported by the National Natural Science Foundation of China (No. 21671060; 2167010747); the Program for Innovative Research Team in Chinese Universities (IRT1237); International Cooperation in Science and Technology Projects of China (2014DFR40480); Applied Technology Research and Development Program Foreign Cooperation Project of Heilongjiang Province (WB15C101).

References

1 S. T. Navale, G. D. Khuspe, M. A. Chougule and V. B. Patil, Camphor sulfonic acid doped PPy/a-Fe_2O_3 hybrid nanocomposites as NO_2 sensors, *RSC Adv.*, 2014, **4**, 27998–28004.

2 Y.-C. Liang and Y.-J. Lo, High-temperature solid-state reaction induced structure modifications and associated photoactivity and gas-sensing performance of binary oxide one-dimensional composite system, *RSC Adv.*, 2017, **7**, 29428–29439.

3 S. T. Navale, D. K. Bandgar, M. A. Chougule and V. B. Patil, Facile method of preparation of PbS films for NO_2 detection, *RSC Adv.*, 2015, **5**, 6518–6527.

4 L. Q. Song, W. Y. Shi and C. Lu, Confinement Effect in Layered Double Hydroxide Nanoreactor: Improved Optical Sensing Selectivity, *Anal. Chem.*, 2016, **88**, 8188–8193.

5 K. P. Gattu, K. Ghule, A. A. Kashale, V. B. Patil, D. M. Phase, R. S. Mane, S. H. Han, R. Sharma and A. V. Ghule, Bio-green synthesis of Ni-doped tin oxide nanoparticles and its influence on gas sensing properties, *RSC Adv.*, 2015, **5**, 72849–72856.

6 G. D. Khuspe, R. D. Sakhare, S. T. Navale, M. A. Chougule, Y. D. Kolekar, R. N. Mulik, R. C. Pawar, C. S. Lee and V. B. Patil, Nanostructured SnO_2 thin films for NO_2 gas sensing applications, *Ceram. Int.*, 2013, **39**, 8673–8679.

7 T. Xie, N. Sullivan, K. Steffens, B. Wen, G. N. Liu, R. Debnath, A. Davydov, R. Gomez and A. Motayed, UV-assisted room-temperature chemiresistive NO_2 sensor based on TiO_2 thin film, *J. Alloys Compd.*, 2015, **653**, 255–259.

8 M. Epifani, E. Comini, R. Díaz, C. Force, P. Siciliano and G. Faglia, TiO_2 colloidal nanocrystals surface modification by V_2O_5 species: investigation by ^{47,49}Ti MAS-NMR and H_2, CO and NO_2 sensing properties, *Appl. Surf. Sci.*, 2015, **351**, 1169–1173.

9 C. Wang, L. L. Guo, N. Xie, X. Y. Kou, Y. F. Sun, X. H. Chuai, S. M. Zhang, H. W. Song, Y. Wang and G. Y. Lu, Enhanced nitrogen oxide sensing performance based on tin-doped tungsten oxide nanoplates by a hydrothermal method, *J. Colloid Interface Sci.*, 2018, **512**, 740–749.

10 D. L. Yan, S. Y. Li, S. Y Liu, M. Tan and M. Cao, Electrodeposited tungsten oxide films onto porous silicon for NO_2 detection at room temperature, *J. Alloys Compd.*, 2018, **735**, 718–727.

11 C. W. Zou, J. Wang and W. Xie, Synthesis and enhanced NO_2 gas sensing properties of ZnO nanorods/TiO_2 nanoparticles heterojunction composites, *J. Colloid Interface Sci.*, 2016, **478**, 22–28.

12 E. Martinelli, D. Polese, A. Catini, A. D. Amico and C. D. Natale, Self-adapted temperature modulation in metal-oxide semiconductor gas sensors, *Sens. Actuators, B*, 2012, **161**, 534–541.

13 J. Courbat, D. Briand, L. Yue, S. Raible and N. F. de Rooij, Drop-coated metal-oxide gas sensor on polyimide foil with reduced power consumption for wireless applications, *Sens. Actuators, B*, 2012, **161**, 862–868.

14 J. Fonollosa, L. Fernández, R. Huerta, A. Gutiérrez-Gálvez and S. Marco, Temperature optimization of metal oxide sensor arrays using mutual information, *Sens. Actuators, B*, 2013, **187**, 331–339.

15 P. Lu, Y. Liu, T. T. Zhou, Q. Wang and Y. S. Li, Recent advances in layered double hydroxides (LDHs) as two-dimensional membrane materials for gas and liquid separations, *J. Membr. Sci.*, 2018, **567**, 89–103.

16 C. L. Tan, X. H. Cao, X.-J. Wu, Q. Y. He, J. Yang, X. Zhang, J. Chen, W. Zhao, S. K. Han, G.-H. Nam, M. Sindoro and H. Zhang, Recent Advances in Ultrathin Two-Dimensional Nanomaterials, *Chem. Rev.*, 2017, **117**, 6225–6331.

17 Y. P. Lin, Y. M. Li, Q. Y. Lan, X.-J. Lv, S. M. Liu, D. Liu and W. T. Hu, A novel strategy for preparing layered double hydroxide/exfoliated carbon nanostructures composites as superior electrochemical catalysts with respect to oxygen evolution and methanol oxidation, *J. Alloys Compd.*, 2018, **744**, 347–356.

18 J. C. Yan, Y. Chen, L. B. Qian, W. G. Gao, D. Ouyang and M. F. Chen, Heterogeneously catalyzed persulfate with a CuMgFe layered double hydroxide for the degradation of ethylbenzene, *J. Hazard. Mater.*, 2017, **338**, 372–380.

19 I. Lee, G. H. Jeong, S. An, S.-W. Kim and S. H. Yoon, Facile synthesis of 3D MnNi-layered double hydroxides (LDH)/graphene composites from directly graphites for pseudocapacitor and their electrochemical analysis, *Appl. Surf. Sci.*, 2018, **429**, 196–202.

20 S. Morandi, F. Prinetto, M. D. Martino, G. Ghiotti, O. Lorret, D. Tichit, C. Malagu, B. Vendemiati and M. C. Carotta, Synthesis and characterisation of gas sensor materials obtained from Pt/Zn/Al layered double hydroxides, *Sens. Actuators, B*, 2006, **118**, 215–220.

21 H. X. Sun, Z. Y. Chu, D. H. Hong, G. Zhang, Y. Xie, L. Li and K. Y. Shi, Three-dimensional hierarchical flower-like Mg-Al-layered double hydroxides: fabrication, characterization and enhanced sensing properties to NO_x at room temperature, *J. Alloys Compd.*, 2016, **658**, 561–568.

22 S. Anandan, C.-Y. Chen and J. J. Wu, Sonochemical synthesis and characterization of turbostratic $MnNi(OH)_2$ layered double hydroxide nanoparticles for supercapacitor applications, *RSC Adv.*, 2014, **4**, 55519–55523.

23 L. Cocheci, L. Lupa, R. Lazau, R. Vod and R. Pode, Zinc recovery from waste zinc ash - a new “green” route for the

preparation of Zn-Al layered double hydroxide used for molybdate retention, *J. Alloys Compd.*, 2019, **787**, 332–343.
24 L. Liu, W. Wang and Y. Hu, Layered double hydroxide-decorated flexible polyurethane foam: significantly improved toxic effluent elimination, *RSC Adv.*, 2015, **5**, 97458–97466.
25 F. A. Rad, Z. Rezvani and F. Khodam, Molecular design confirmation for proposition of improved photophysical properties in a dye intercalated layered double hydroxides, *RSC Adv.*, 2016, **6**, 11193–11203.
26 Z. Z. Yang, F. H. Wang, C. Zhang, G. G. Zeng, X. F. Tan, Z. G. Yu, Y. Zhong, H. Wang and F. Cui, Utilization of LDH-based materials as potential adsorbents and photocatalysts for the decontamination of dyes wastewater: a review, *RSC Adv.*, 2016, **6**, 79415–79436.
27 X. H. Zhou, H. Chen, Q. H. Chen and Q. D. Ling, Synthesis and characterization of two-component acidic ion intercalated layered double hydroxide and its use as a nanoflame-retardant in ethylene vinyl acetate copolymer (EVA), *RSC Adv.*, 2017, **7**, 53064–53075.
28 N. Almoisheer, F. A. Alseroury, R. Kumar, M. Aslam and M. A. Barakat, Adsorption and anion exchange insight of indigo carmine onto CuAl-LDH/SWCNTs nanocomposite: kinetic, thermodynamic and isotherm analysis, *RSC Adv.*, 2019, **9**, 560–568.
29 D. H. Hong, J. W. Zhang, A. U. Rehmana, L. H. Gong, J. Zhou, K. Kan, L. Li and K. Y. Shi, One-step synthesis of hierarchical Ni-Fe-Al layered double hydroxide with excellent sensing properties for NO_x at room temperature, *RSC Adv.*, 2016, **6**, 103192–103198.
30 D. M. Xu, M. Y. Guan, Q. H. Xu and Y. Guo, Multilayer films of layered double hydroxide/polyaniline and their ammonia sensing behavior, *J. Hazard. Mater.*, 2013, **262**, 64–70.
31 Y. X. Qin, L. P. Wang and X. F. Wang, Hierarchical layered double hydroxides with Ag nanoparticle modification for ethanol sensing, *Nanotechnology*, 2018, **29**, 1361–6528.
32 D. M. Xu, M. Y. Guan, Q. H. Xu and Y. Guo, Multilayer films of layered double hydroxide/polyaniline and their ammonia sensing behavior, *J. Hazard. Mater.*, 2013, **262**, 64–70.
33 G. Y. Kang, Z. Zhu, B. H. Tang, C. H. Wu and R. J. Wu, Rapid detection of ozone in the parts per billion range using a novel Ni–Al layered double hydroxide, *Sens. Actuators, B*, 2017, **241**, 1203–1209.
34 H. J. Li, X. Y. Su, C. H. Bai, Y. Q. Xu, Z. C. Pei and S. G. Sun, Detection of carbon dioxide with a novel HPTS/NiFe-LDH nanocomposite, *Sens. Actuators, B*, 2016, **225**, 109–114.
35 L. P. Zhu, Z. Wen, W. M. Mei, Y. G. Li and Z. Z. Ye, Porous CoO Nanostructure Arrays Converted from Rhombic Co(OH)F and Needle-like $Co(CO_3)0.5(OH)\cdot 0.11H_2O$ and their Electrochemical Properties, *J. Phys. Chem. C*, 2013, **117**, 20465–20473.
36 M. S. Faber, R. Dziedzic, M. A. Lukowski, N. S. Kaiser, Q. Ding and S. Jin, High-Performance Electrocatalysis Using Metallic Cobalt Pyrite (CoS_2) Micro- and Nanostructures, *J. Am. Chem. Soc.*, 2014, **136**, 10053–10061.
37 Y. Q. Zhang, B. O. Yang, J. Xu, G. C. Jia, S. Chen, R. S. Rawat and H. J. Fan, Rapid Synthesis of Cobalt Nitride Nanowires: Highly Efficient and Low-Cost Catalysts for Oxygen Evolution, *Angew. Chem., Int. Ed.*, 2016, **55**, 8670–8674.
38 Z. Y. Wang, J. T. Li, X. C. Tian, X. P. Wang, Y. Yu, K. A. Owusu, L. He and L. Q. Mai, Porous Nickel−Iron Selenide Nanosheets as Highly Efficient Electrocatalysts for Oxygen Evolution Reaction, *ACS Appl. Mater. Interfaces*, 2016, **8**, 19386–19392.
39 S. F. Shen, M. L. Xu, D. B. Lin and H. B. Pan, The growth of urchin-like Co_3O_4 directly on sensor substrate and its gas sensing properties, *Appl. Surf. Sci.*, 2017, **396**, 327–332.
40 J. Li, M. Wei, W. Chu and N. Wang, High-stable a-phase NiCo double hydroxide microspheres via microwave synthesis for supercapacitor electrode materials, *Chem. Eng. J.*, 2017, **316**, 277–287.
41 Z. B. Tian, Q. Y. Li, J. Y. Hou, L. Pei, Y. Li and S. Y. Ai, Platinum nanocrystals supported on CoAl mixed metal oxide nanosheets derived from layered double hydroxides as catalysts for selective hydrogenation of cinnamaldehyde, *J. Catal.*, 2015, **331**, 193–202.
42 L. P. Xu, Y.-S. Ding, C.-H. Chen, L. L. Zhao, C. Rimkus, R. Joesten and S. L. Suib, 3D Flowerlike r-Nickel Hydroxide with Enhanced Electrochemical Activity Synthesized by Microwave-Assisted Hydrothermal Method, *Chem. Mater.*, 2008, **20**, 308–316.
43 F. Peng, H. Li, D. H. Wang, P. Tian, Y. X. Tian, G. Y. Yuan, D. M. Xu and X. Y. Liu, Enhanced Corrosion Resistance and Biocompatibility of Magnesium Alloy by Mg-Al-Layered Double Hydroxide, *ACS Appl. Mater. Interfaces*, 2016, **8**, 35033–35044.
44 S.-D. Jiang, L. Song, W.-R. Zeng, Z.-Q. Huang, J. Zhan, A. A. Stec, T. R. Hull, Y. Hu and W. Zhao, Self-Assembly Fabrication of Hollow Mesoporous Silica@Co−Al Layered Double Hydroxide@Graphene and Application in Toxic Effluents Elimination, *ACS Appl. Mater. Interfaces*, 2015, **7**, 8506–8514.
45 J. H. Fang, M. Li, Q. Q. Li, W. F. Zhang, Q. L. Shou, F. Liu, X. B. Zhang and J. P. Cheng, Microwave-assisted synthesis of CoAl-layered double hydroxide/graphene oxide composite and its application in supercapacitors, *Electrochim. Acta*, 2012, **85**, 248–255.
46 M. Li, K. Y. Ma, J. P. Cheng, D. H. Lv and X. B. Zhang, Nickel-cobalt hydroxide nanoflakes conformal coating on carbon nanotubes as a supercapacitive material with high-rate capability, *J. Power Sources*, 2015, **286**, 438–444.
47 Y. F. Zhao, Q. Wang, T. Bian, H. J. Yu, H. Fan, C. Zhou, L.-Z. Wu, C.-H. Tung, D. O'Harec and T. Zhang, Ni^{3+} doped monolayer layered double hydroxide nanosheets as efficient electrodes for supercapacitors, *Nanoscale*, 2015, **7**, 7168–7173.
48 G. G. Zhang, S. H. Zang and X. C. Wang, Layered $Co(OH)_2$ Deposited Polymeric Carbon Nitrides for Photocatalytic Water Oxidation, *ACS Catal.*, 2015, **5**, 941–947.
49 J. Yang, H. W. Liu, W. N. Martens and R. L. Frost, Synthesis and Characterization of Cobalt Hydroxide, Cobalt Oxyhydroxide, and Cobalt Oxide Nanodiscs, *J. Phys. Chem. C*, 2010, **114**, 111–119.

50 Y. L. Ge, K. Kan, Y. Yang, L. Zhou, L. Q. Jing, P. K. Shen, L. Li and K. Y. Shi, Highly mesoporous hierarchical nickel and cobalt double hydroxide composite: fabrication, characterization and ultrafast NO_x gas sensors at room temperature, *J. Mater. Chem. A*, 2014, **2**, 4961–4969.

51 D. Y. Deng, X. X. Xing, N. Chen, Y. X. Lia and Y. D. Wang, Hydrothermal synthesis of β-$Co(OH)_2$ nanoplatelets: a novel catalyst for CO oxidation, *J. Phys. Chem. Solids*, 2017, **100**, 107–114.

52 G. L. Fan, H. Wang, X. Xiang and F. Li, Co-Al mixed metal oxides/carbon nanotubes nanocomposite prepared via a precursor route and enhanced catalytic property, *J. Solid State Chem.*, 2013, **197**, 14–22.

53 S. Ahmad, M. Kharkwal, Govind and R. Nagarajan, Application of $KZnF_3$ as a Single Source Precursor for the Synthesis of Nanocrystals of ZnO_2:F and ZnO:F; Synthesis, Characterization, Optical, and Photocatalytic Properties, *J. Phys. Chem. C*, 2011, **115**, 10131–10139.

54 Z. Zhao, Y. L. Xu, M. D. Ji and H. Zhang, Synthesis and electrochemical performance of F-doped $Li_4Ti_5O_{12}$ for lithium-ion batteries, *Electrochim. Acta*, 2013, **109**, 645–650.

55 Z. Z. Liang, Z. Y. Yang, Z. H. Huang, J. Qi, M. X. Chen, W. Zhang, H. Q. Zheng, J. L. Sun and R. Cao, Novel insight into the epitaxial growth mechanism of six-fold symmetrical β-$Co(OH)_2$/Co(OH)F hierarchical hexagrams and their water oxidation activity, *Electrochim. Acta*, 2018, **271**, 526–536.

56 J. Liu, X. Y. Li, Q. D. Zhao, J. Ke, H. N. Xiao, X. J. Lv, S. M. Liu, M. Tadé and S. B. Wang, Mechanistic investigation of the enhanced NH_3-SCR on cobalt-decorated Ce-Ti mixed oxide: in situ FTIR analysis for structure-activity correlation, *Appl. Catal., B*, 2017, **200**, 297–308.

57 C. Fang, L. Y. Shi, H. Hu, J. P. Zhang and D. S. Zhang, Rational design of 3D hierarchical foam-like Fe_2O_3@CuO_x monolith catalysts for selective catalytic reduction of NO with NH_3, *RSC Adv.*, 2015, **5**, 11013–11022.

58 H. Xu, J. W. Zhang, A. U. Rehman, L. H. Gong, K. Kan, L. Li and K. Y. Shi, Synthesis of NiO@CuO nanocomposite as high-performance gas sensing material for NO_2 at room temperature, *Appl. Surf. Sci.*, 2017, **412**, 230–237.

59 P. F. Liu, S. Yang, B. Zhang and H. G. Yang, Defect-Rich Ultrathin Cobalt−Iron Layered Double Hydroxide for Electrochemical Overall Water Splitting, *ACS Appl. Mater. Interfaces*, 2016, **8**, 34474–34481.

60 B. Zhang, M. Cheng, G. N. Liu, Y. Gao, L. J. Zhao, S. Li, Y. P. Wang, F. M. Liu, X. S. Liang, T. Zhang and G. Y. Lu, Room temperature NO_2 gas sensor based on porous Co_3O_4 slices/reduced graphene oxide hybrid, *Sens. Actuators, B*, 2018, **263**, 387–399.

61 D. M. Han, L. L. Zhai, F. B. Gu and Z. H. Wang, Highly sensitive NO_2 gas sensor of ppb-level detection based on In_2O_3 nanobricks at low temperature, *Sens. Actuators, B*, 2018, **262**, 655–663.

62 B. U. Wojcik, T. A. Vincent, M. F. Chowdhury and J. W. Gardner, Ultrasensitive WO_3 gas sensors for NO_2 detection in air and low oxygen environment, *Sens. Actuators, B*, 2017, **239**, 1051–1059.